International Journal of Advanced Engineering and Technology Research
ISSN: 3106-8677 (Print), ISSN: 3106-8685 (Online) | Vol. 1, No. 3, 2026

Wheat LAI Inversion and Yield Estimation under T-MLP

Huan Li

School of Surveying and Land Information Engineering, Henan Polytechnic University, Jiaozuo 454000, China

Abstract: To address the limited accuracy and poor generalization capabilities of existing winter wheat Leaf Area Index (LAI) inversion methods, such as the NDVI vegetation index model and support vector machine (SVM), this paper proposes a hybrid modeling approach that integrates a radiative transfer model with deep learning. This method uses the PROSAIL model to generate simulated samples, optimizes the input parameter configuration through local and global sensitivity analysis, constructs a lookup table (LUT) to assist in the generation of training sets, and designs a T-MLP network that integrates Transformer and Multilayer Perceptron (MLP). This approach leverages the cross-band global dependencies in Landsat 8multispectral data and enhances LAI modeling capabilities through nonlinear regression. Using ground-truth data from the main wheat-producing region of Shangqiu City, Henan Province, this model's performance is validated and compared with the NDVI, PROSAIL and CNN models. Winter wheat yield estimation is then performed using the LAI inverted by the T-MLP model in combination with the EC-LUE model. Results showed that T-MLP achieved superior inversion accuracy across multiple growth stages (R^2=0.83, RMSE=1.04), outperforming the NDVI model (R^2=0.55, RMSE=1.58), the PROSAIL model (R^2=0.76, RMSE=1.36) and CNN model (R^2=0.78, RMSE=1.12). Comparison of the inversion results with the MODIS LAI product revealed that T-MLP demonstrated greater robustness in terms of temporal consistency and cross-plot stability, accurately reflecting the dynamic trends of wheat LAI. The relative error of yield predictions was below 10%. This study provides a practical approach for high-precision LAI inversion and yield estimation that integrates physical constraints with the advantages of deep learning.

Keywords: Winter wheat, leaf area index, PROSAIL, Transformer, MLP.

1. Introduction

As China's most important food crop, winter wheat's growth and stable yield are crucial for ensuring national food security. The leaf area index (LAI), a key parameter for measuring wheat's photosynthetic capacity and growth, is one of the core indicators reflecting changes in arable land productivity [1–5]. Therefore, timely acquisition of LAI values for winter wheat at different growth stages is crucial for scientifically assessing wheat growth, predicting yield, providing early warning for food security, and supporting macroeconomic regulation of agriculture [6–11].

At present, the main methods for obtaining LAI include field measurement and remote sensing data inversion. Field measurement has the advantage of accurate local measurement, but the spatial representativeness of point scale is poor, and it is time-consuming and labor-intensive to carry out a large amount of related work. Using remote sensing data to invert LAI has become the main means at present, such as statistical models based on vegetation index [12] and physical models based on radiation transfer theory. With the rapid development of AI technology, deep learning models have been widely used in remote sensing LAI inversion. Zhu et al [13] used a multilayer perceptron (MLP) neural network model based on Sentinel-2 data to estimate the mean tilt angle (MTA) of crop canopy structure parameters. The results showed that the B6 band of Sentinel-2 has a strong correlation with MTA. Zhang et al [14] improved the accuracy of inversion when inverting soybean LAI using multi-source images combined with support vector machine (SVM), MLP and other neural network models. Yao et al [15] et al. inverted the LAI of corn based on multispectral imagery from drones. The results showed that the accuracy of LAI inversion during the entire growth period based on random forest (RF) was superior to that at other spatial scales. Wu [16] et al. used Sentinel-2 data combined with the Gaussian process regression (GPR) algorithm of machine learning (ML) to estimate the leaf area index of rice during multiple growth periods. However, the lack of mechanistic support in the above studies resulted in weak interpretability and transferability. The physical model is based on the theory of vegetation canopy radiation transfer and constructs a quantitative relationship between surface spectral reflectance and physiological parameters such as LAI. The model has a clear physical mechanism support, strong applicability, and is not easily restricted by crop types and regional conditions. Wang et al [17] et al. used the PROSAIL model to establish a lookup table (LUT) to invert the LAI of silage corn, improving the inversion performance. Li et al [18] used a hybrid method of PROSAIL and machine learning to significantly improve the accuracy of LAI estimation. Li [19] used PROSAIL model simulation data combined with measured data and then used RF and partial least squares regression (PLSR) machine learning algorithms to invert LAI, which was more accurate than the traditional PROSAIL model. Although the above-mentioned inversion methods using PROSAIL have achieved good results, they have problems such as complex models, multiple parameters, strong dependence on input data quality, and in-depth exploration of the relationship between LAI and band values. In addition, the phenomenon of "different parameters but same effect" is prone to occur, which affects the accuracy of the inversion results.

In recent years, with the continuous improvement of the spatiotemporal resolution and accuracy of remote sensing data and meteorological data, many scholars have made progress in exploring crop yield estimation. Li et al [20] established six rice yield estimation models and completed the estimation of rice yield per unit area in Chongqing, with an accuracy rate of 85% and good overall results. However, a large amount of measured data is required. Fu et al. [21] used the WOFOST model to estimate corn yield and achieved a high yield estimation accuracy. However, the WOFOST model has too many parameters, and the debugging of the model is time-consuming and labor-intensive. Guo et al. [22] used remote sensing parameters such as LAI and combined them with the VMD-GRU model to estimate winter wheat yield. The correlation reached an extremely significant level ($P < 0.01$), and its accuracy was better than that of a single yield estimation model. But there is a phenomenon of low yield estimation results in the estimation of high-yield samples. Zhang Lei et al [23]. developed a BO-CNN-BiLSTM (BCBL) model, combining the feature extraction capabilities of 1DCNN with the time-series memory advantages of Bidirectional Long Short-Term Memory (BiLSTM) networks. They combined data such as the Vegetation Enhancement Index (EVI) and LAI to estimate winter wheat yield in Henan Province, achieving high estimation accuracy. Li Changchun [24] et al. developed a CNN-MALSTM estimation model that captures information from input sequences in different feature subspaces, enhancing the model's expressive power. They constructed an annual yield distribution map of Henan Province. Cross-validation was used to evaluate the model's stability in different years. Results showed that the CNN-MALSTM model can provide stable yield estimates. Zhang Chishan [25] et al. developed a phenology-guided Bayesian convolutional neural network (PB-CNN) framework for county-level crop yield estimation and uncertainty quantification, using soybeans in the US Corn Belt as a case study. Results showed that the PB-CNN framework significantly enhanced our understanding of the complex response of soybean yield to different environmental conditions at different phenological stages and the associated uncertainties, leading to more sustainable agricultural development.

Therefore, this paper proposes a hybrid LAI inversion method that integrates PROSAIL and T-MLP neural networks. Combining physical constraints with the advantages of deep learning, this method uses sensitivity analysis to determine parameter ranges, constructs a lookup table to optimize training data, and uses the Transformer to capture the global dependence of spectral coupling between multiple Landsat 8 bands. The MLP enhances nonlinear representation capabilities. The accuracy of the model was compared with that of the NDVI vegetation index model, the PROSAIL model, and the CNN neural network model. The inverted LAI is combined with the EC-LUE model to estimate winter wheat yield. Validation is conducted on experimental plots and measured data. Results demonstrate that this method combines the simplicity of empirical models with the noise immunity of physical models.

2. Materials and Methods

2.1. Study Area

Three 15 km x 15 km experimental study areas were selected (shown in Figure 1): Zhecheng County (blue frame), Yucheng County (black frame), and Yongcheng City (red frame) in Henan Province. Their geographic coordinates range from 34°07′N to 34°47′N, and 115°16′E to 116°39′E. They are in the core agricultural region of the Huanghuai Plain and have a typical warm temperate monsoon climate. The study areas have an average elevation of 30 to 50 m, are flat, and are primarily alluvial plains. With abundant water resources, these areas are ideal for crop growth. Wheat and corn are the primary crops grown in the area, using a wheat-summer corn rotation system. Wheat is typically planted in October and harvested in June.

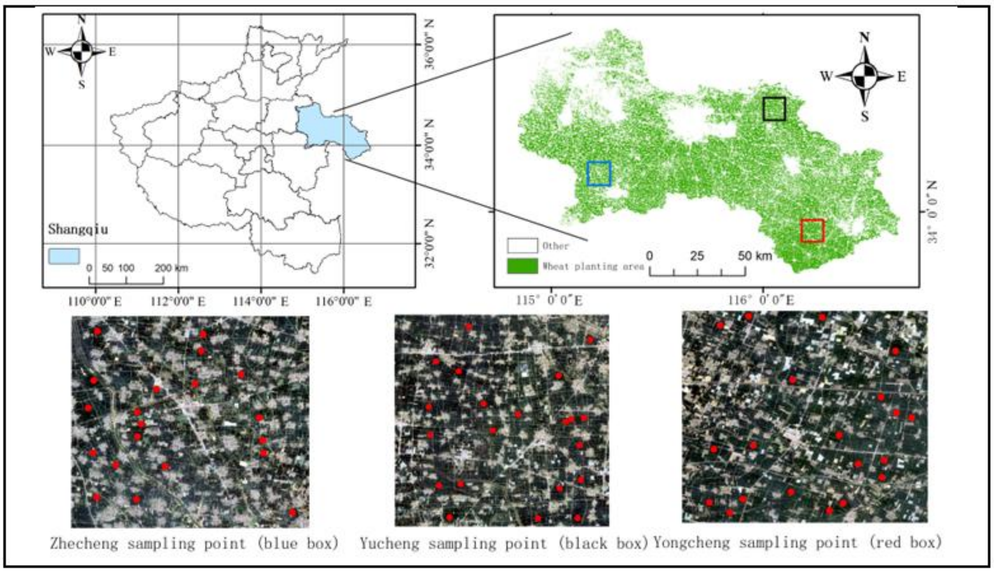

Zhecheng sampling point (blue box) Yucheng sampling point (black box) Yongcheng sampling point (red box)

Figure 1. Location of the study area, wheat planting area and distribution of sampling points

2.2. Data Collection

2.2.1. Ground Truth Data

Surveying and mapping operations were conducted using the Key Laboratory of Mine Spatiotemporal Information and Ecological Restoration of the Ministry of Natural Resources at Henan Polytechnic University, People's Republic of China. The LAI 2000 plant canopy analyzer was used to measure the LAI of winter wheat in the study area on the ground. Measurements were made on February 24 (greening period), March 24 (jointing period), April 20 (heading period), and May 15 (maturity period) in 2024. To ensure data representativeness, 20 sampling points were evenly selected across the study area (as shown in Figure 1) and accurately positioned and marked using a GNSS positioning system. Data collection was performed under clear, cloudless, light winds, and good visibility weather conditions. Consistency was maintained during measurements to ensure comparability between different sampling points. After eliminating outliers, 18 valid LAI measurements were obtained per month for each study area.

2.2.2. Remote Sensing Data and Preprocessing

Landsat 8 imagery data, launched by the U.S. Geological Survey (USGS), is equipped with an Oli/TIRS sensor and includes 11 spectral bands covering multiple spectral ranges, including visible, near-infrared (NIR), short-wave infrared (SWIR), and thermal infrared (TIR). It is widely used in studies such as land use/land cover change, vegetation monitoring, and water analysis. The spatial resolution of the imagery varies depending on the band, with a resolution of 30m for the visible and near-infrared bands and 100m for the thermal infrared band. This imagery has a large coverage area and a short revisit period (16 days), uses the UTM-WGS84 projection coordinate system, and outputs data in GeoTIFF format. Preprocessing steps include radiometric calibration, atmospheric correction, and geometric correction. After processing, appropriate bands can be selected for analysis based on the image's spectral characteristics. Based on the image's spectral characteristics, bands B3, B4, B5, B6, and B7 of the Landsat 8 imagery were selected before winter wheat leaf area index retrieval. The corresponding band information is shown in Table 1.

Table 1. Introduction to some bands of Landsat 8 images

spectral bands	Wavelength range/μm	Resolution /m	Use
B3	0.53~0.59	30	Vegetation classification
B4	0.64~0.67	30	Chlorophyll absorption
B5	0.85~0.88	30	Estimating vegetation cover
B6	1.56~1.66	30	Estimation of soil and vegetation moisture content
B7	2.10~2.28	30	Identifying soil moisture

2.3. Model

2.3.1. PROSAIL Radiative Transfer Model

The PROSAIL radiation transfer model combines the PROSPECT leaf optical model with the bidirectional reflectance SAIL model of vegetation canopy and is widely used in remote sensing research fields such as vegetation canopy parameter inversion [26–32]. The PROSPECT model assumes that leaves have a multi-layer structure and a rough surface. Based on the biochemical characteristics of the leaves (such as chlorophyll concentration (C_{ab}), leaf dry matter concentration (C_m), leaf equivalent water thickness (C_w), leaf structural parameters (N_s), leaf tilt distribution parameters (θ), etc.) as input, the reflectance and transmittance of the leaves in different bands are calculated through a complex simulation process. The PROSPECT formula is:

$$R_{leaf}(\lambda)=f(C_{ab}, C_m, C_w, N_s, \theta, \lambda) \qquad (1)$$

Where: $R_{leaf}(\lambda)$ is the reflectivity of the leaf, and λ is the wavelength.

The SAIL model assumes that the vegetation canopy is composed of uniformly distributed leaves, all of which have the same optical properties in all directions. The model uses the radiation transfer equation to simulate the optical behavior of the canopy through the radiation transfer process of multiple scattering and reflection. The leaf reflectivity and transmittance calculated by the PROSPECT model are input into the SAIL model. The SAIL model can reproduce the radiation transfer process within the vegetation canopy and calculate the reflectivity of the vegetation canopy. The formula is:

$$P(\lambda)=\text{PROSAIL}\left(N_s, C_{ab}, C_{ar}, C_w, C_m, C_{brown}, V_{LIDF}, V_{LAI}, H, \theta_s, \theta_v, \varphi_v, \rho_\gamma\right) \qquad (2)$$

Where $P(\lambda)$ is the reflectance of the vegetation canopy at wavelength, C_{ar} is the red chlorophyll concentration, C_{brown} is the leaf brown matter concentration, V_{LIDF} is the leaf tilt distribution function, V_{LAI} is the leaf area index, H is the canopy height, θ_s is the solar incidence angle, θ_v is the relative leaf inclination angle, φ_v is the solar radiation azimuth, and ρ_γ is the background reflectance.

PROSPECT calculates the reflectivity and transmittance of leaves and inputs them into the SAIL model to simulate the reflectivity of the entire vegetation canopy. The combined formula is:

$$P_{final}(\lambda)=\text{SAIL}(\text{PROSPECT}\Big(C_{ab}, C_m, C_w, N_s, \theta, \lambda) C_{ar}, C_{brown}, V_{LIDF}, V_{LAI}, H, \theta_s, \theta_v, \varphi_v, \rho_\gamma\Big) \qquad (3)$$

Where: $P_{final}(\lambda)$ is the final calculated vegetation canopy reflectance.

2.3.2. Sensitivity Analysis and Lookup Table Construction

Sensitivity analysis is a method used to assess the sensitivity of model output to changes in input parameters. It is divided into global sensitivity analysis and local sensitivity analysis according to the scope of analysis. Local sensitivity analysis is mainly used to evaluate the impact of changes in a single input parameter on the model output within a specific parameter space. Common methods include the one-variable-at-a-time method (OAT) and parameter sensitivity coefficients. The OAT method assumes that other input parameters remain unchanged and examines the response of a specific parameter change to the model results. Because the PROSAIL model contains multiple parameters and is affected by regional differences, the coupling effect between parameters may cause errors in the model prediction results. Therefore, this study will use the OAT method in local sensitivity analysis to conduct sensitivity analysis on the model's input parameters and complete the localization of the parameters.

When inverting vegetation using physical models, the inversion problem often arises due to the larger number of uncertain parameters in the model than the observed parameters, and the nonlinear relationship between vegetation biochemical parameters and spectral reflectance. Lookup tables (LUTs) offer an effective solution. To create an effective LUT, this paper uses the step size method to generate the LUT. For example, for chlorophyll concentration C_{ab}, the range is [0, 100] mg/m2, and the step size is set to 5 mg/m2, generating 20 different chlorophyll concentration values (0, 5, 10, ..., 100). For other parameters, the same appropriate step size is used for discretization. For each discretized input parameter combination, the PROSAIL model is used to simulate and calculate the vegetation canopy reflectance in the corresponding band. For each input parameter combination (N_s, C_{ab}, C_{ar}), the PROSAIL model outputs the corresponding reflectance, generating a total of 13,384 data sets that form the content of the LUT. The LUT is in Excel format, and the 6 columns of data are the simulated LAI value, B3, 4, 8, 11, and 12 band values.

2.3.3. T-MLP Model

The T-MLP hybrid model combines the global modeling capabilities of the Transformer with the nonlinear expression capabilities of the MLP. The LUT is introduced into the T-MLP hybrid regression model as an auxiliary training data source. The regression model constructed in this paper consists of two parts: a Transformer encoder and a multi-layer perceptron (MLP) regression head. The overall architecture is shown in Figure 2:

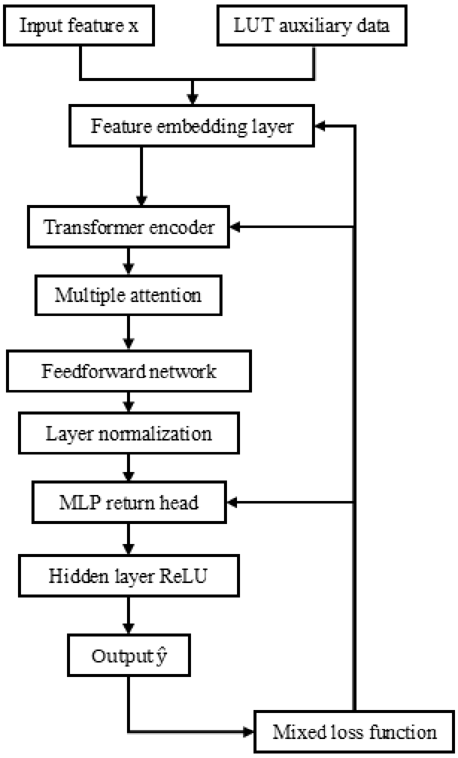

Figure 2. Flowchart of the T-MLP hybrid regression model

In the input feature embedding layer, the original feature dimension d is usually small, and the input is first mapped to a high-dimensional space through a linear mapping.

$$Z_0=x\cdot W_e+b_e, W_e\in R^{d\times d_{model}} \tag{4}$$

Where: d_{model} is the encoding dimension of Transformer, W_e and b_e are learnable parameters.

The Transformer encoder is mainly composed of a multi-head self-attention mechanism and a feedforward network, which can automatically model the global interaction relationship between each input feature. In the multi-head attention mechanism, the formula for calculating the self-attention of the input sequence is:

$$\text{Attention}(Q, K, V)=\text{softmax}\left(\frac{QK^T}{\sqrt{d_k}}\right)V \tag{5}$$

Where: $Q=z_0W^Q$, $K=z_0W^K$, $V=z_0W^V$, $d_k=\frac{d_{model}}{h}$ is the dimension of each attention head;

The multi-head mechanism splices multiple heads together:

$$\text{MultiHead}(Z_0)=\text{Concat}(\text{head}_1\ldots,\text{head}_h)\cdot W^o \tag{6}$$

The final output $Z_L\in R^{d_{model}}$ represents the global semantics of the input features.

The Transformer output encoding vector Z_L is connected to an MLP regression head to enhance nonlinear mapping capabilities. Assume that the MLP contains L layers and its structure is:

$$h^0=Z_L \tag{7}$$

$$h^{(l)}=\sigma\left(h^{(l-1)}W^{(l)}+b^{(l)}\right), l=1, \ldots, L-1 \tag{8}$$

$$\hat{y}=h^{(L-1)}\cdot W^{(L)}+b^{(L)} \tag{9}$$

Where $\sigma(\cdot)$ represents the ReLU activation function.

Taking into account both large error sensitivity and robustness, a combination of MSE and L1 loss is used:

$$L(y,\hat{y})=\alpha\cdot(y-\hat{y})^2+(1-\alpha)\cdot|y-\hat{y}| \tag{10}$$

Set α to 0.5, and the final optimization goal is to minimize the average loss of training samples:

$$\min_{\theta}\frac{1}{N}\sum_{i=1}^{N} L\left(y_i,f(x_i;\theta)\right) \tag{11}$$

2.4. LAI inversion Method

The generated LUT is used as the data basis and imported into the T-MLP hybrid regression model for LAI inversion modeling. The Transformer module is used to learn the global dependencies between bands, and MLP regression enhances the nonlinear fitting ability of the model. The specific steps are to extract the reflectance data of B3, 4, 8, 11, and 12 in the image as input features, corresponding to the simulated bands in the LUT. The band data extracted from the remote sensing image is calibrated to convert the original value of each pixel into a standard reflectance value. The reflectance values of all bands are limited to the range of [0.0001, 1.0], and then the data is normalized.

During the training phase, the backpropagation algorithm was used to minimize the combined loss function (a hybrid of MSE and L1). Parameters were updated using the AdamW optimizer, with an initial learning rate of 0.001 and a cosine annealing learning rate schedule. The data was divided into an 80% training set and a 20% validation set, with a maximum number of training epochs of 200. Early stopping was used to prevent overfitting.

During the model prediction phase, the input is the multi-band reflectance characteristics of each pixel in the remote sensing image, and the output is the corresponding LAI value. The prediction results are denormalized to actual physical units and linearly adjusted to ensure they are within a reasonable ecological range. The LAI prediction results are written to a TIFF file.

2.5. Accuracy Evaluation

The coefficient of determination (R^2) and root mean square error (RMSE) were used as evaluation indicators of model accuracy.

$$R^2=1-\frac{\sum_{i=1}^{n}(K_i-J_i)^2}{\sum_{i=1}^{n}(K_i-\bar{K})^2} \tag{12}$$

$$\text{RMSE}=\sqrt{\frac{1}{n}\sum_{i=1}^{n}(K_i-J_i)^2} \tag{13}$$

Where K_i is the predicted value, J_i is the actual value, $\overline{K}$ is the mean of the predicted values, and n is the number of samples. The LAI results obtained from modeling and inversion were validated and evaluated for accuracy. An R^2 value closer to 1 indicates a better model fit; a smaller RMSE value indicates lower inversion error and higher accuracy.

3. Results

3.1. Sensitivity Analysis

The OAT local sensitivity analysis method was used to analyze the input parameters of the PROSAIL model. The results are shown in Figure 3. In the visible light band, as C_{ab} increases, the spectral reflectance gradually decreases, and after the 780 nm band, the canopy reflectance basically remains unchanged. As C_{ar} increases, the canopy reflectance decreases slightly within the 500-560 nm band and remains essentially unchanged in other bands. As C_m increases, the canopy reflectance remains essentially unchanged before the 780 nm band, but decreases significantly after that. As C_w increases, the canopy reflectance remains essentially unchanged between the 500-780 nm band and gradually decreases between the 780-2500 nm band. As N_s increases, the canopy reflectance changes slightly across the entire band. LAI changes across the entire band, with an increase in LAI causing a slight increase in the 730-1300 nm band and a significant decrease in the remaining bands. Through OAT quantitative analysis: in the band range of 500-780nm, LAI and C_{ab} have a greater impact on the spectral reflectivity; in the band of 780-1300nm, C_m has the greatest impact on the spectral reflectivity; in the band of 1500-2500nm, C_w and LAI contribute more to the spectral reflectivity, θ_s and H have slight changes between 750nm and 1300nm, and basically no changes in other bands.

Based on the Extended Fourier Amplitude Sensitivity Test (EFAST), this study conducted a systematic global sensitivity analysis on key input parameters in the PROSAIL radiative transfer model to reveal the contribution mechanism and coupling effect of various biophysical parameters in the simulation of vegetation canopy spectra. Within the parameter range determined in Table 2, 13,384 sets of parameter samples were randomly generated using the Markov Chain Chain Monte Carlo (MCMC) method, and the corresponding canopy reflectance spectra were obtained by simulating the PROSAIL forward model. Then, based on the EFAST method, the first-order and all-order (total) sensitivity of leaf structure parameters (N), chlorophyll content (C_{ab}), carotenoid content (C_{ar}), anthocyanin content (C_{ant}), dry matter content (C_m), equivalent water thickness (C_w), leaf area index (LAI), leaf tilt angle distribution function (LIDF), and soil background reflectance (P_{siol}) to the simulated reflectance were quantitatively evaluated. The first-order sensitivity results (Figure 4a) show that in the visible light band (400–780 nm), LAI and C_{ab} are the dominant factors in the spectral response, contributing a combined total of over 80%. In the near-infrared region (780–1400 nm), C_m makes the most significant contribution (approximately 60%), followed by LAI and C_m. In the short-wave infrared regions I (1400–1900 nm) and II (1900–2500 nm), the dominant factors shift to C_w (approximately 60%) and LAI (approximately 60%), respectively, and C_w and C_m also exhibit significant influence in each band. Notably, the first-order sensitivity of C_{ab} approaches zero beyond 780 nm, confirming the spectral mechanism that chlorophyll absorption characteristics are mainly limited to the visible light region. The full-order sensitivity results (Figure 4b) further reveal the complex interactions between parameters: across the entire spectrum, all parameters exhibit varying degrees of coupling effects, ranked by coupling contribution as follows: LAI > C_w > C_m >C_{ab} > P_{siol} > N > LIDF > C_{ar} > C_{ant}. The cumulative coupling contributions of the four parameters LAI, C_w, C_m, and C_{ab} exceed 80%, highlighting their central role in the model output variation. Sensitivity analysis not only deepens the understanding of the spectral response mechanism of the PROSAIL model but also provides key parameter optimization and constraint basis for the subsequent construction of a high-precision, highly interpretable LAI inversion model.

During model training, parameters such as LAI, C_{ab}, and C_m significantly affect canopy reflectance in specific bands, indicating that they play an important role in LAI prediction. In the subsequent model training process, these key parameters are preferentially selected as input features. Based on the ground-based measured data and the quantitative results of parameter sensitivity analysis, the input parameters and their value ranges of the PROSAIL model are determined. With reference to prior knowledge in related fields [17], some parameter values are reasonably set, as shown in Table 2.

Table 2. Input parameters and value ranges of the PROSAIL model

Model	Parameter	Numerical	Step length
PROSPECT	N_s	1~3.2	0.1
	$C_{ab}/(mol\cdot L^{-1})$	10~100	5
	$C_{ar}/(mol\cdot L^{-1})$	2~20	2
	$C_m/(mol\cdot L^{-1})$	0.002~0.02	0.001
	C_w/cm	0.001~0.041	0.005
SAIL	V_{LAI}	0.5~7	0.5
	V_{LIDF}	Ellipsoid distribution function	
	θ_s/(°)	20~80	5
	ρ_γ	0.2	
	H	0.1~1	0.05

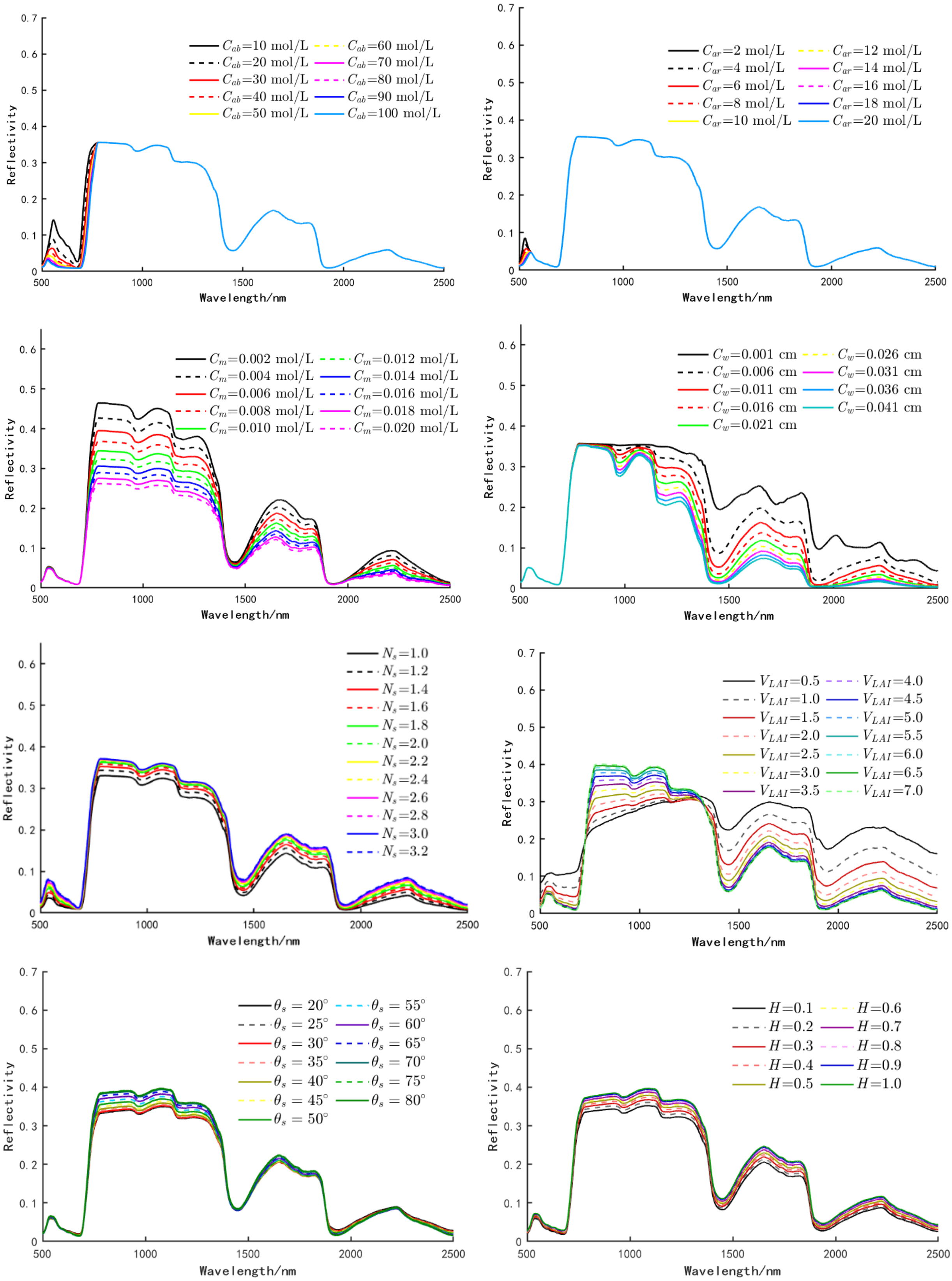

Figure 3. Local sensitivity analysis results of PROSAIL model parameters

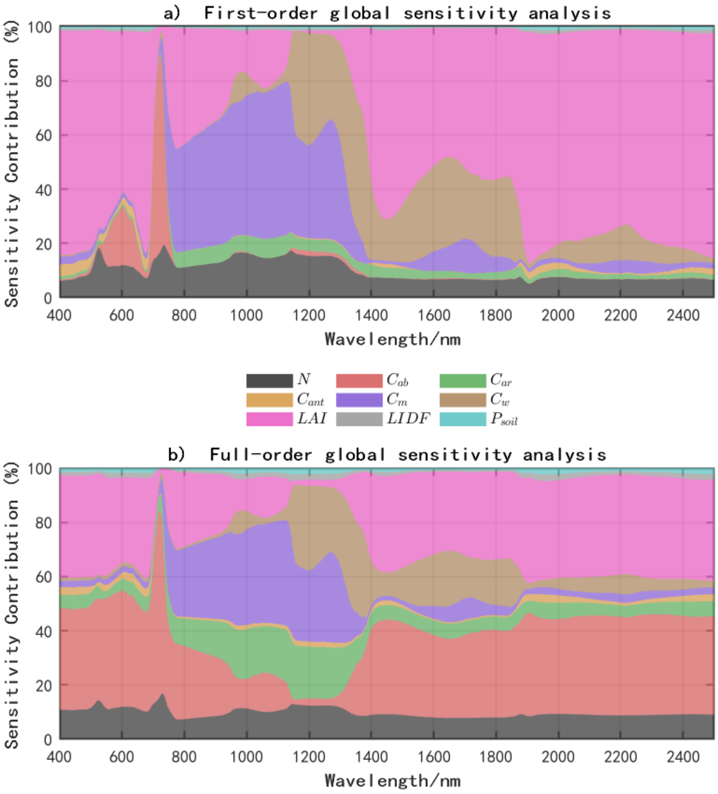

Figure 4. First-order (a) and global (b) sensitivity analysis

3.2. Model Accuracy Analysis

The NDVI empirical model, PROSAIL physical model, and T-MLP hybrid model were selected, and the corresponding data were used for modeling analysis to compare the modeling accuracy of the three methods. Among them: the logarithmic model listed in the reference [33] of the NDVI empirical model has the following formula:

$$\mathrm{NDVI}=\frac{\mathrm{B8-B4}}{\mathrm{B8+B4}} \tag{14}$$

$$\mathrm{LAI}=e^{1.426+\frac{-0.542}{\mathrm{NDVI}}} \tag{15}$$

Figure 4 plots the training loss and validation set RMSE. Initially (in the first 20 epochs), the training loss decreases rapidly, allowing the model to quickly learn the basic mapping between reflectivity and LAI. The loss then slowly decreases, reaching convergence after 80 epochs. The RMSE on the validation set remains low, fluctuating within a narrow range without a significant upward trend, indicating that the model is not overfitting and exhibits good generalization. The RMSE remains stable between epochs 50 and 150, confirming the effectiveness of the early stopping strategy. The T-MLP hybrid model maintains learning capabilities while maintaining robustness.

The modeling accuracy is shown in Table 3 and Figure 5. Table 3 shows that the NDVI empirical model has a poor modeling accuracy of 0.55, while the PROSAIL model improves the R² by 0.21 compared to the NDVI model. The accuracy of CNN models has improved. The T-MLP neural network model has higher modeling accuracy than both the NDVI empirical model and the PROSAIL physical model, with the R² increasing from 0.76 for the PROSAIL model to 0.83. As shown in Figure 6, the T-MLP inversion results show an overall linear relationship, indicating high model training accuracy. This model effectively improves the accuracy of LAI predictions, demonstrating stronger fitting capabilities and lower prediction errors compared to the traditional NDVI empirical model and the single PROSAIL model.

Table 3. Model accuracy table

Model Type	R^2	RMSE
NDVI empirical model	0.5531	1.5856
PROSAIL model	0.7611	1.3625
T-MLP model	0.8301	1.0401
CNN model	0.7811	1.1244

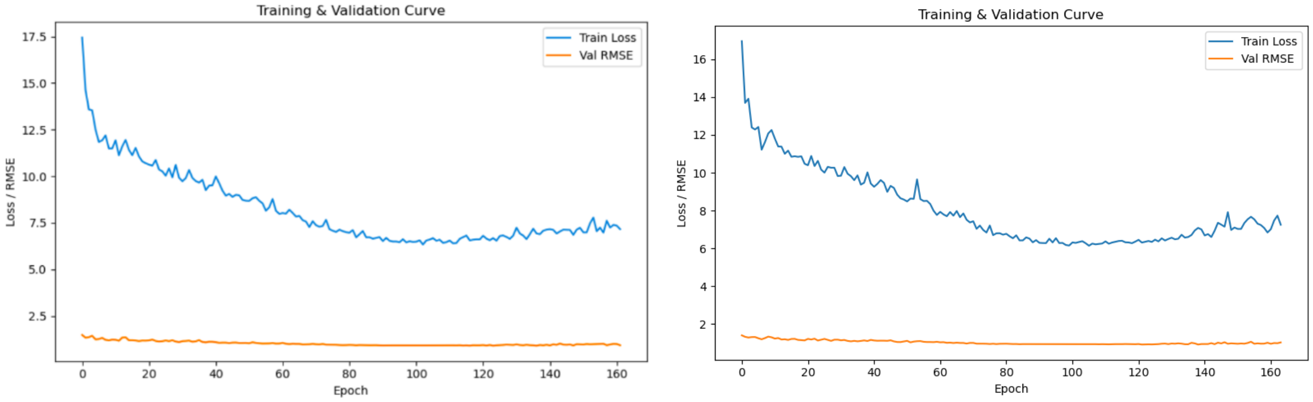

Figure 5. T-MLP (left) and CNN (right) model training loss and RMSE change curve

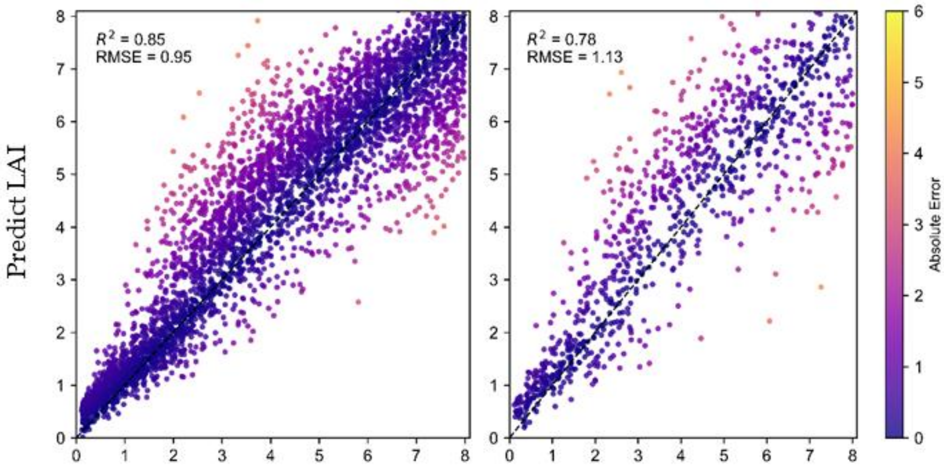

Simulated LAI value (training set) Simulated LAI value (test set)

Figure 6. T-MLP modeling accuracy table for the study area (unit: m2/m2)

3.3. Inversion Result Analysis

3.3.1. Single-point Accuracy Verification

The accuracy of the measured and inverted values was verified under different models, and the results are shown in Figures 6-9.

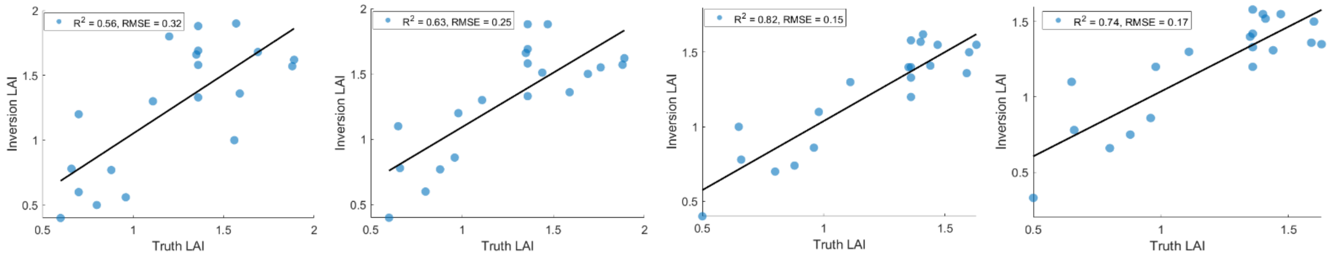

NDVI empirical model PROSAIL model T-MLP model CNN model

Figure 7. Measurement verification results on February 24

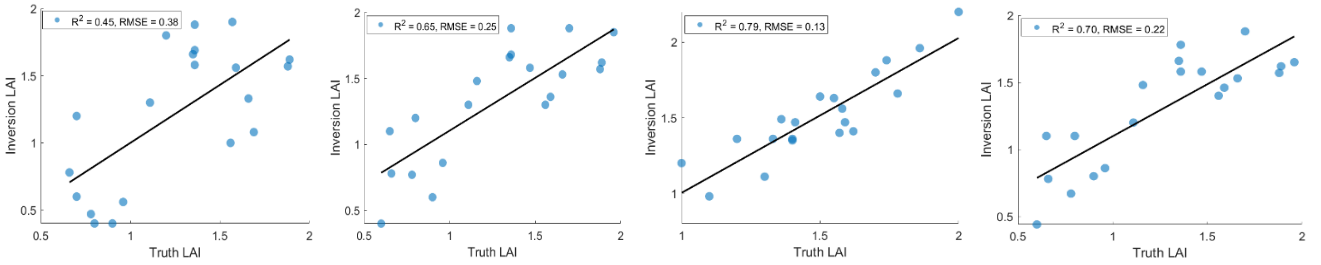

NDVI empirical model PROSAIL model T-MLP model CNN model

Figure 8. Measurement verification results on March 24

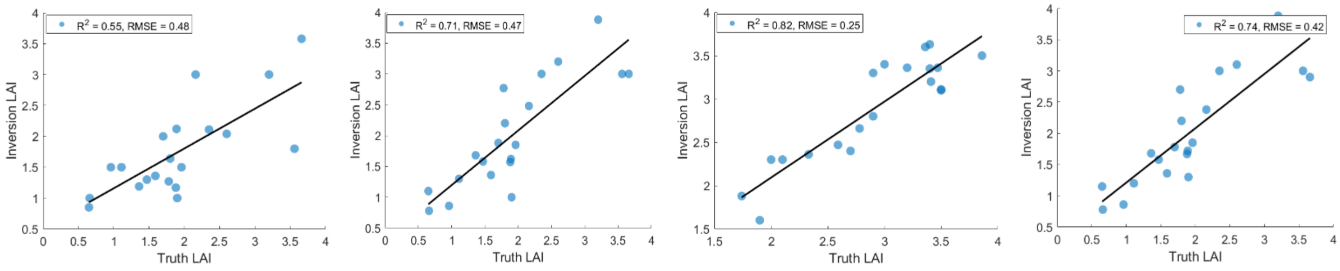

NDVI empirical model PROSAIL model T-MLP model CNN model

Figure 9. Measurement verification results on April 20

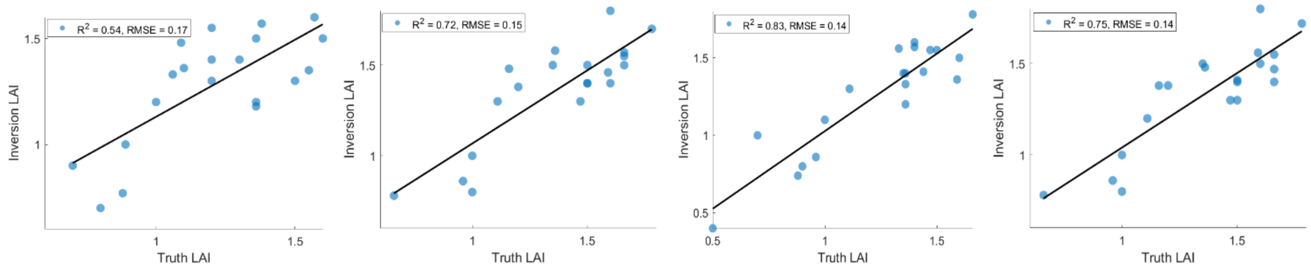

NDVI empirical model PROSAIL model T-MLP model CNN model

Figure 10. Measurement verification results on May 15

In February, wheat gradually turned green, and the measured LAI ranged from 0 to 2. As shown in Figure 7, the NDVI empirical model had low accuracy, with an R² of 0.56. The LAI distribution was generally scattered, with some points slightly underestimated. The PROSAIL model was more accurate than the NDVI empirical model, with an R² of 0.63, and a more pronounced linear correlation between measured and predicted LAI values. The CNN model has an R² score of 0.74 and an RMSE of 0.17. The inversion accuracy is improved after adding the CNN neural network model. The T-MLP model achieved the highest accuracy, with an R² of 0.82, a 0.19 improvement over the PROSAIL model and the best linear fit.

In March, wheat was in its growing season, and LAI measurements ranged from 0 to 2.3, with the mode concentrated between 1 and 2.2. Overall, LAI values increased compared to February. In Figure 8, the vegetation index model showed slightly lower accuracy, with an R² of 0.45. The data were not concentrated, resulting in poor prediction performance. The PROSAIL model achieved an R² of 0.65, showing improved accuracy, The CNN model has an R² of 0.70 and an RMSE of 0.22. but with significant underestimation of individual points. The T-MLP model achieved an R² of 0.79, a 0.14 point improvement over the PROSAIL model. The linear correlation was more pronounced, with slight data dispersion, but overall performance was superior to both the NDVI and PROSAIL models.

In April, wheat was at the jointing stage, and measured LAI values ranged from 0.6 to 3.9, with a mode of 2.2. These values were generally higher than those in March. In Figure 9, the vegetation index model's prediction accuracy remained poor, with an R² of 0.51. In comparison, the PROSAIL model achieved an R² of 0.71, showing improved accuracy. The CNN model has an R² of 0.74 and an RMSE of 0.42. Its inversion performance is more accurate than the PROSAIL model. The data were partially discrete, while the T-MLP model achieved an R² of 0.82, demonstrating better overall accuracy. This is because as wheat grew and developed in April, the spectral reflectance gradually saturated and stabilized, leading to better predictions using the hybrid model.

In May, wheat plant height growth has completed and the grain filling stage has begun. At the time of measurement, the wheat was mature and its leaves had turned yellow. Therefore, the measured values decreased compared to April, as shown in Figure 10. The values ranged from 0 to 1.87, with a concentration between 1.2 and 1.6. In May, the vegetation index model achieved an R² of 0.54, while the PROSAIL model achieved an R² of 0.72, a 0.11 improvement over the vegetation index model. The CNN model has an R² of 0.75 and an RMSE of 0.14. The T-MLP model achieved an R² of 0.83, a 0.11 improvement over the PROSAIL model. The measured values ranged from 0 to 1.87, with an overall low RMSE, indicating high LAI prediction accuracy.

Verification results from February to May show that the T-MLP model outperformed both the PROSAIL model and the NDVI vegetation index model, with a relatively small gap between modeling and verification accuracy. Due to the saturation of NDVI, the vegetation index models performed poorly, with significant data discrepancy and poor overall accuracy. While the PROSAIL model's accuracy improved compared to the NDVI vegetation index model, it still fell short of ideal performance. The T-MLP model automatically learned effective feature representations from the input data, improving prediction accuracy and significantly increasing the algorithm's speed, demonstrating its superior data simulation capabilities.

3.3.2. LAI Inversion Map

The T-MLP neural network model was used to invert the leaf area index of winter wheat in the three experimental areas at different periods, and the LAI inversion maps from February to May were generated.

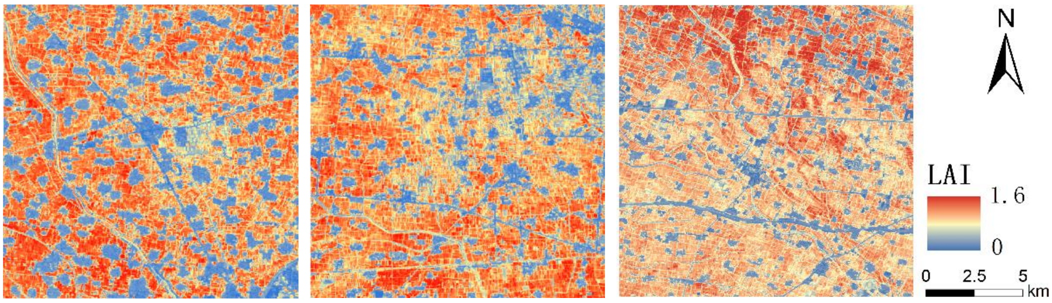

Zhecheng Yucheng Yongcheng

Figure 11. LAI inversion maps of the three test areas on February 24

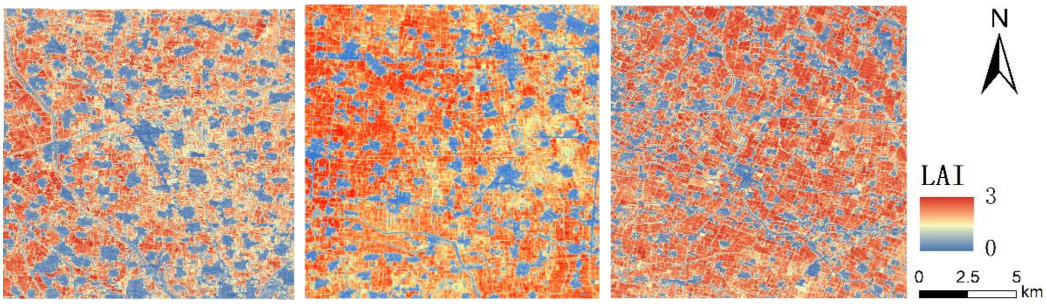

Zhecheng Yucheng Yongcheng

Figure 12. LAI inversion maps of the three test areas on March 24

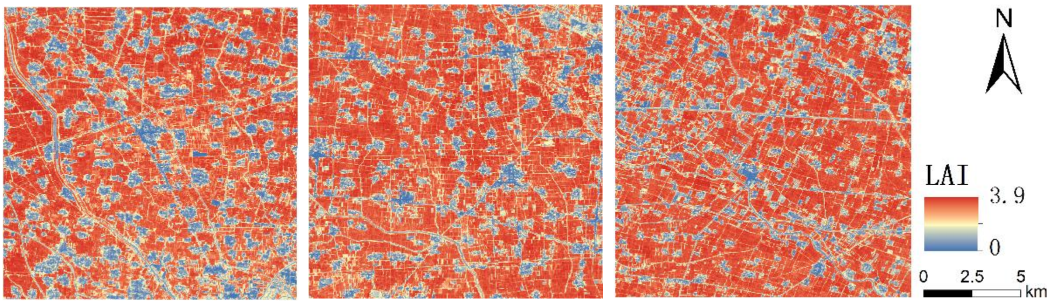

Zhecheng Yucheng Yongcheng

Figure 13. LAI inversion maps of the three test areas on April 20

Zhecheng Yucheng Yongcheng

Figure 14. LAI inversion maps of the three test areas on May 15

As shown in Figure 11, wheat planting and irrigation began earlier in the eastern part of the study area than in the western part. Therefore, the inverted LAI values for winter wheat in the study area in mid-to-late February appear slightly higher in the east and lower in the west. Most LAI values in the study area in February were concentrated around 1.4, indicating that wheat was in its greening phase. LAI values for towns, water bodies, and roads were less than 0.2. Some inverted LAI values were slightly higher than the measured values. The mean LAI of the measured points in February was 0.94, while the inverted mean was 1.21, with a deviation of 0.25. The overall deviation was consistent with expectations, and the inverted results generally accurately reflect the growth status of wheat. In February, March, and April, wheat was in the greening, jointing (Figure 12), and heading stages (Figure 13), respectively. The LAI value gradually increased, and the overall LAI was higher in areas with high vegetation coverage. In mid-to-late May, wheat gradually matured (Figure 14), and the leaves gradually changed from green to yellow. The overall LAI decreased compared to April. The measured mean value in May was 1.36, and the inverted mean value was 1.58, indicating a good overall fit.

3.4. LAI Comparative Analysis

To verify the accuracy and stability of the model, a temporal comparison analysis was performed between MODIS LAI and LAI retrieved using the T-MLP model. The MODIS LAI (MOD15A2H) product is a global vegetation LAI remote sensing product acquired by the MODIS sensors on NASA's Terra and Aqua satellites. Its spatial resolution is 500 meters, and a product is generated every eight days [34–37]. A temporal comparison analysis of LAI fitting between MODIS LAI and LAI retrieved using the PROSAIL-MLP hybrid model was performed from February to May, as shown in Figures 15-17.

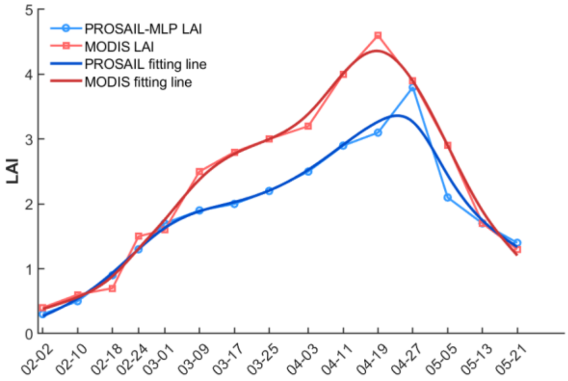

Figure 15. Zhecheng Time Series LAI Line Chart

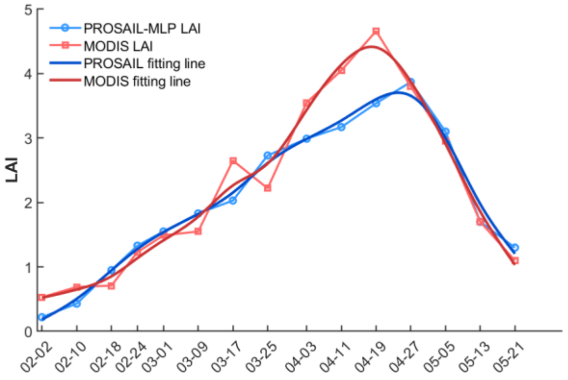

Figure 16. Yucheng Time Series LAI Line Chart

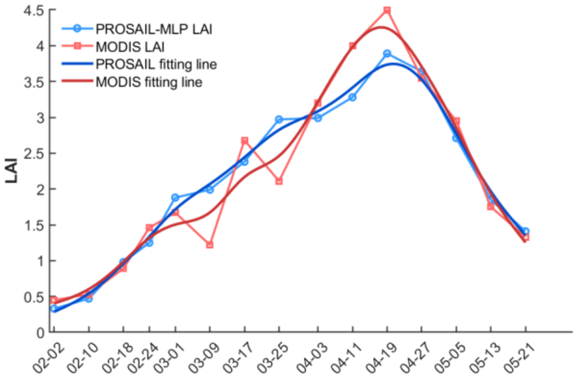

Figure 17. Yongcheng Time Series LAI Line Chart

As shown in the figure, LAI increases slowly from early February to mid-March, during the period between greening and jointing. It rises rapidly from late March to mid-April, during the period of rapid growth (jointing to heading). LAI peaks in late April, reaching maximum values of approximately 4.6 and 3.9 in both the MODIS and T-MLP curves, corresponding to the period from heading to early grain filling. Subsequently, as wheat matures, chlorophyll content decreases, and leaf color gradually shifts from green to yellow, the LAI rapidly declines. Both LAI inversions from the two data sets accurately reflect the typical growth cycle of winter wheat, but the T-MLP model's LAI shows a smoother trend and better matches the temporal variation of wheat LAI.

3.5. Production Estimation Using LAI Inversion Model Combined with EC-LUE Model

3.5.1. EC-LUE Yield Estimation Model

Based on the wheat LAI on April 20 (heading period) obtained by inversion from the T-MLP model, the Eddy covariance light use efficiency (EC-LUE) model [38] was used to estimate the wheat yield distribution in the three study areas.

Calculate the gross primary productivity (GPP) of vegetation and then convert the GPP value into crop yield using the following formula:

$$\text{Yield}=\text{GPP}*\text{AR}*\frac{1}{1+\text{RS}}*\frac{1}{1\text{-MC}}*\text{HI} \tag{16}$$

Where Yield represents winter wheat yield; AR is the available carbon remaining after plant respiration, which is 0.64; RS is the ratio of aboveground to belowground biomass, which is 0.2; MC is the grain moisture content, which is 0.12; and HI is the ratio of aboveground biomass to grain. To simulate the GPP of winter wheat in the study area, the specific formula is:

$$\text{GPP}=\text{PAR}*\text{fPAR}*\varepsilon_{\max}*\min(T_s,W_s) \tag{17}$$

$$\text{fPAR}=a*\text{LAI}+b \tag{18}$$

$$T_s=\frac{(T-T_{\min})*(T-T_{\max})}{(T-T_{\min})*(T-T_{\max})-(T-T_{\text{opt}})^2} \tag{19}$$

$$W_s=\frac{\text{VPD}_{\max}-\text{VPD}}{\text{VPD}_{\max}-\text{VPD}_{\min}} \tag{20}$$

Where PAR is photosynthetically active radiation, set at 8.5 MJ/m²/day; fPAR is the fraction of photosynthetically active radiation absorbed by vegetation; $\varepsilon_{\max}$ is the maximum light energy utilization efficiency, set at 2.16 gC/(m²*MJ); T_s and W_s represent the temperature and water stress functions, respectively. LAI is the leaf area index, and a and b are empirical coefficients. T is the current temperature, $T_{\min}$, $T_{\max}$ and T_{opt} are the minimum, maximum, and optimum temperatures for plant photosynthesis, set at 0°C, 40°C, and 22°C, respectively. VPD is the current atmospheric vapor pressure deficit, with $\text{VPD}_{\max}$ and $\text{VPD}_{\min}$ representing the maximum and minimum saturation vapor pressure deficit (VPD), respectively, at 4200 Pa and 640 Pa.

3.5.2. Analysis of Production Estimation Results

Based on the LAI inverted from the T-MLP model, the wheat yield distribution of the three study areas was simulated using the EC-LUE model as shown in Figure 18 (unit: 103 kg/ha).

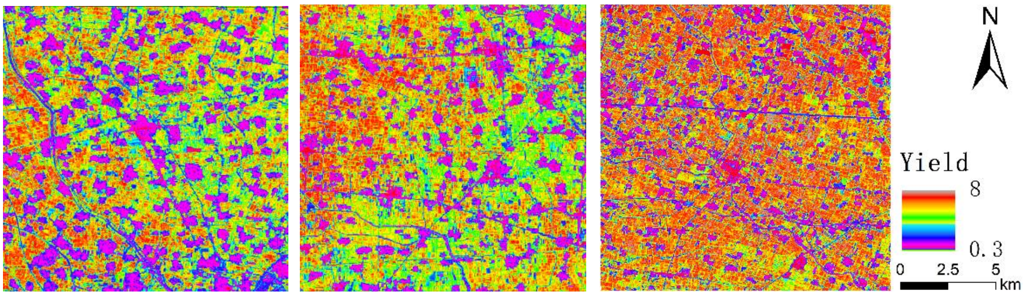

Zhecheng Yucheng Yongcheng

Figure 18. Yield distribution map of the study area

Figure 17 shows that the inverted yields in southwestern Zhecheng County and northwestern Yucheng County are relatively high. The inverted yields in Yongcheng City are relatively evenly distributed overall, but the high-yield areas are more dispersed. Low values are distributed in areas such as towns, roads, and buildings, which is consistent with local conditions.

Based on the wheat planting distribution map (Figure 1), the inverted wheat yield mean for each study area was calculated. A comparative analysis with the corresponding actual yield mean is shown in Table 4.

Table 4. Estimated and actual yields (unit: 10^3 kg/ha)

	Estimated average production	Actual mean	Relative error
Zhecheng	6.975	7.582	-8.01%
Yucheng	6.733	7.427	-9.34%
Yongcheng	7.814	7.271	7.45%

Table 4 shows that the EC-LUE model-based yield estimates show some overestimation and underestimation, but the relative errors are within 10%, indicating that the model can effectively infer winter wheat yield. This demonstrates the effectiveness of the T-MLP model in inverting LAI, and the results provide experience and reference for regional-scale crop growth monitoring and yield estimation.

4. Discussion

By combining the PROSAIL radiation transfer model with the T-MLP hybrid neural network model, high-precision inversion of winter wheat LAI at the regional scale was achieved. Winter wheat yield was then inverted using LAI in conjunction with the EC-LUE model. Results show that compared to the NDVI empirical model, CNN model and single-physics models, the T-MLP hybrid model performs better in terms of regression accuracy, generalization, and the ability to express nonlinear relationships. In terms of modeling, the Transformer module can model the global dependencies between multi-band reflectances, while the MLP component effectively enhances the fitting capabilities of nonlinear mappings. The combination of the two enables the model to handle complex spectral patterns while avoiding overfitting. The high accuracy of yield prediction indirectly demonstrates the accuracy and stability of the T-MLP model.

Overall trend analysis shows that both MODIS and T-MLP-derived LAI well reflect the typical growth cycle characteristics of winter wheat. However, the pixel values of the MODIS leaf area index product fluctuate significantly over time, with numerous peaks and troughs. The overall LAI values of the curve are slightly higher than those of the T-MLP model, with a particularly pronounced difference during the main growing season (March-April). This discrepancy may be due to the larger spatial resolution (500m) of MODIS, which results in pixel-by-pixel effects, and the longer temporal compositing period (8 days), which smooths out actual field-scale variations. T-MLP, based on Landsat 8 imagery, has a spatial resolution of 20m, far exceeding the 500m resolution of MODIS, effectively avoiding pixel-by-pixel effects. As shown in Figures 14-16, the T-MLP model shows smoother and more reasonable LAI trends across wheat growth stages, providing a better indirect depiction of wheat growth and decline. Its response to LAI increases during the main growing season (March-April) is more consistent with wheat's physiological logic.

The T-MLP model demonstrated good fitting accuracy and spatial restoration capabilities across different counties, with an estimated yield error of approximately 10%. The model demonstrated stable generalization performance. Compared to traditional linear statistical or empirical models, the T-MLP model more fully exploits the nonlinear characteristics of remote sensing time series data and effectively reflects the complex ecological and environmental response mechanisms during crop growth.

The study still has limitations. Regarding LAI inversion, although sampling points were relatively evenly distributed across the study area, the number of samples in some plots was insufficient, potentially leading to slightly lower model accuracy in some areas, particularly at the edges of highly heterogeneous plots. The T-MLP model performed well overall, but errors were present at individual points during the greening and grain filling periods. This may be due to the low or high LAI values during these periods, and the spectral signal from remote sensing images is susceptible to interference from soil background or reflectance changes caused by yellowing leaves. Future efforts will include the introduction of vegetation index combinations or spectral degradation compensation strategies to improve model stability in extreme LAI ranges. Yield estimates show slight overestimations and underestimations. This is due to the uncertainty of LAI inverted by remote sensing, particularly in areas with blurred plot boundaries or a high concentration of mixed vegetation pixels. The input meteorological data (such as PAR and VPD) are ERA5 reanalysis products, which may exhibit resolution mismatch near township boundaries.

Current research focuses primarily on the T-MLP model, but its performance under different ecological conditions and timescales has yet to be fully evaluated. As research deepens, future studies will incorporate multi-regional, multi-year LAI and yield data for validation, aiming to improve the model's adaptability and stability under diverse environmental conditions.

5. Conclusions

This paper proposes a T-MLP hybrid model that integrates a radiative transfer model with deep learning to invert LAI, and combines it with the EC-LUE model to estimate winter wheat yield. Results show that the LAI inverted by the T-MLP model outperforms the empirical NDVI model and the PROSAIL physical model across multiple growing stages, with a maximum R^2 of 0.83 and a minimum RMSE of 0.32. The hybrid model is capable of handling complex band relationships and has excellent fitting capabilities. The LAI inverted images show clear spatial structure and growing stage differences across different plots, validating the model's applicability for cross-regional application. In areas with relatively flat terrain and similar cropping practices, the model has the potential for direct transfer and application. Comparison with the MODIS LAI product shows that the T-MLP model better reflects the dynamic evolution of winter wheat from greening, jointing, heading, to grain filling in the temporal dimension, with less oversmoothing or jumps, avoiding the mixed pixel errors common in medium- and low-resolution products.

When the inverted LAI was used for yield estimation, the mean relative error of the estimated yield in three counties (Zhecheng, Yucheng, and Yongcheng) was within 10%, demonstrating good yield reliability. This also indirectly demonstrates the accuracy of the T-MLP model in inverting LAI. Compared with empirical models and single-physics models, T-MLP offers a flexible structure and high modeling efficiency. It can effectively capture the complex nonlinear relationship between LAI and band values, and has great potential for widespread application. It provides a practical method for inverting remote sensing parameters, regional agricultural monitoring, and precision management.

References

[1] Min H.E.; Jianguang W.E.N.; Dongqing Y.O.U.; Yong T.; Shengbiao W.U.; Dalei H.A.O.; Xingwen L.I.N.; Zhangrong G. Review of forest Leaf Area Index retrieval over rugged terrain based on remotely sensed data. Natl. Remote Sens. Bull. 2022, 26, 2451–2472, doi:10.11834/jrs.20210244.

[2] JIANG H.; JIA K.; ZHAO X.; WEI X.; WANG B.; YAO Y.; ZHANG X.; JIANG B. Review on the theory, method, and research progress of leaf area index estimation in mountainous areas. Natl. Remote Sens. Bull. 2020, 24, 1433–1449, doi:10.11834/jrs.20200229.

[3] Tian, Y.; Jiang, Y.; Zeng, M.; Hui, J.; Jiang, Q. Inversion of Cotton Leaf Area Index under Verticillium Wilt Stress from UAV Multispectral Images: Deep Learning-Based vs. Classical-Based Algorithms. Ind. Crops Prod. 2025, 233, 121345, doi:10.1016/j.indcrop.2025.121345.

[4] Mulero, G.; Bonfil, D.J.; Helman, D. Wheat Leaf Area Index Retrieval from Drone-Derived Hyperspectral and LiDAR Imagery Using Machine Learning Algorithms. Agric. For. Meteorol. 2025, 372, 110648, doi:10.1016/j.agrformet.2025.110648.

[5] Guo, J.; Zeng, X.; Ma, Q.; Yuan, Y.; Zhang, N.; Lin, Z.; Yin, P.; Yang, H.; Liu, X.; Zhang, F. UAV-Based Yield Prediction Based on LAI Estimation in Winter Wheat (Triticum Aestivum L.) Under Different Nitrogen Fertilizer Types and Rates. Plants 2025, 14, 1986, doi:10.3390/plants14131986.

[6] Fu, W.; Chen, Z.; Cheng, Q.; Li, Y.; Zhai, W.; Ding, F.; Kuang, X.; Chen, D.; Duan, F. Maize Leaf Area Index Estimation Based on Machine Learning Algorithm and Computer Vision. Agriculture 2025, 15, 1272, doi:10.3390/agriculture15121272.

[7] Vishwakarma, S.K.; Bhattarai, B.; Kothari, K.; Pandey, A. Intercomparison of Machine Learning Models for Estimating Leaf Area Index of Rice Using UAV-Based Multispectral Imagery. Phys. Chem. Earth Parts ABC 2025, 140, 103977, doi:10.1016/j.pce.2025.103977.

[8] Yang, Q.; Zhou, J.; Zhao, L.; Jin, Z. NeRF-LAI: A Hybrid Method Combining Neural Radiance Field and Gap-Fraction Theory for Deriving Effective Leaf Area Index of Corn and Soybean Using Multi-Angle UAV Images. Remote Sens. Environ. 2025, 328, 114844, doi:10.1016/j.rse.2025.114844.

[9] Wu, Q.; Hou, D.; Xie, M.; Gao, Q.; Li, M.; Hao, S.; Cui, C.; Fan, K.; Zhang, Y.; Zhang, Y. Enhanced Spring Wheat Soil Plant Analysis Development (SPAD) Estimation in Hetao Irrigation District: Integrating Leaf Area Index (LAI) Under Variable Irrigation Conditions. Agriculture 2025, 15, 1372, doi:10.3390/agriculture15131372.

[10] Li, H.; Li, Q.; Yu, C.; Luo, S. Unified Estimation of Rice Canopy Leaf Area Index over Multiple Periods Based on UAV Multispectral Imagery and Deep Learning. Plant Methods 2025, 21, 73, doi:10.1186/s13007-025-01398-1.

[11] Yin, G.; Verger, A.; Qu, Y.; Zhao, W.; Xu, B.; Zeng, Y.; Liu, K.; Li, J.; Liu, Q. Retrieval of High Spatiotemporal Resolution Leaf Area Index with Gaussian Processes, Wireless Sensor Network, and Satellite Data Fusion. Remote Sens. 2019, 11, 244, doi:10.3390/rs11030244.

[12] Dongyan Z.; Xuanxuan H.; Fenfang L.; Shizhou D.; Gan Z.; Qi H. Estimation of winter wheat leaf area index using multi-source UAV image feature fusion. Trans. Chin. Soc. Agric. Eng. Trans. CSAE 2022, 38, 171–179, doi:10.11975/j.issn.1002-6819.2022.09.018.

[13] Zhu Sunan. Estimation of crop canopy structural parameters based on Sentinel-2 band. Master's thesis, Nanjing University of Information Science and Technology, 2024.

[14] Zhang Yi. Soybean Leaf Area Index Retrieval Based on UAV Hyperspectral, Multispectral, and LiDAR Remote Sensing Images. Master's Thesis, Yunnan University, 2024.

[15] Yao, Y.; Wang, H.; Yang, X.; Gao, X.; Yang, S.; Zhao, Y.; Li, S.; Zhang, X.; Liu, Z. Interpretable LAI Fine Inversion of Maize by Fusing Satellite, UAV Multispectral, and Thermal Infrared Images. Agriculture 2025, 15, 243, doi:10.3390/agriculture15030243.

[16] Wu, T.; Zhang, Z.; Wang, Q.; Jin, W.; Meng, K.; Wang, C.; Yin, G.; Xu, B.; Shi, Z. Estimating Rice Leaf Area Index at Multiple Growth Stages with Sentinel-2 Data: An Evaluation of Different Retrieval Algorithms. Eur. J. Agron. 2024, 161, 127362, doi:10.1016/j.eja.2024.127362.

[17] WANG Yanlong, W.J. Inversion of Leaf Area Index of Silage Corn Based on PROSAIL Model. Nongye Jixie XuebaoTransactions Chin. Soc. Agric. Mach. 2024, 55.

[18] Li, S.; Lin, Y.; Zhu, P.; Jin, L.; Bian, C.; Liu, J. Combining UAV Multispectral Imaging and PROSAIL Model to Estimate LAI of Potato at Plot Scale. Agriculture 2024, 14, 2159, doi:10.3390/agriculture14122159.

[19] Li Pingping. Winter wheat LAI inversion based on spiking-hybrid method and machine learning. Chinese Agricultural Information 2024, 36, 29–44.

[20] Fan, L.; Fang, S.; Fan, J.; Wang, Y.; Zhan, L.; He, Y. Rice Yield Estimation Using Machine Learning and Feature Selection in Hilly and Mountainous Chongqing, China. Agriculture 2024, 14, 1615, doi:10.3390/agriculture14091615.

[21] Fu, G.; Li, C.; Liu, W.; Pan, K.; He, J.; Li, W. Maize Yield Estimation Based on UAV Multispectral Monitoring of Canopy LAI and WOFOST Data Assimilation. Eur. J. Agron. 2025, 168, 127614, doi:10.1016/j.eja.2025.127614.

[22] Guo, F.; Wang, P.; Tansey, K.; Zhang, Y.; Li, M.; Liu, J.; Zhang, S. A Novel Transformer-Based Neural Network under Model Interpretability for Improving Wheat Yield Estimation Using Remotely Sensed Multi-Variables. Comput. Electron. Agric. 2024, 223, 109111, doi:10.1016/j.compag.2024.109111.

[23] Zhang, L.; Li, C.; Wu, X.; Xiang, H.; Jiao, Y.; Chai, H. BO-CNN-BiLSTM Deep Learning Model Integrating Multisource Remote Sensing Data for Improving Winter Wheat Yield Estimation. Front. Plant Sci. 2024, 15, 1500499, doi:10.3389/fpls.2024.1500499.

[24] Li, C.; Zhang, L.; Wu, X.; Chai, H.; Xiang, H.; Jiao, Y. Winter Wheat Yield Estimation by Fusing CNN–MALSTM Deep Learning with Remote Sensing Indices. Agriculture 2024, 14, 1961, doi:10.3390/agriculture14111961.

[25] Zhang, C.; Diao, C. A Phenology-Guided Bayesian-CNN (PB-CNN) Framework for Soybean Yield Estimation and Uncertainty Analysis. ISPRS J. Photogramm. Remote Sens. 2023, 205, 50–73, doi:10.1016/j.isprsjprs.2023.09.025.

[26] Démoulin, R.; Gastellu-Etchegorry, J.-P.; Lefebvre, S.; Briottet, X.; Zhen, Z.; Adeline, K.; Marionneau, M.; Le Dantec, V. Modeling 3D Radiative Transfer for Maize Traits Retrieval: A Growth Stage-Dependent Study on Hyperspectral Sensitivity to Field Geometry, Soil Moisture, and Leaf Biochemistry. Remote Sens. Environ. 2025, 327, 114784, doi:10.1016/j.rse.2025.114784.

[27] Qiu, L.; Ke, X.; Sun, X.; Lu, Y.; Shi, S.; Liu, W. Investigating the Influence of the Weed Layer on Crop Canopy Reflectance and LAI Inversion Using Simulations and Measurements in a Sugarcane Field. Remote Sens. 2025, 17, 2014, doi:10.3390/rs17122014.

[28] Wang Linfeng. Remote Sensing Assessment of Soybean Waterlogging in Typical Areas of Jilin Province Based on PROSAIL. Master's Thesis, Jilin University, 2025.

[29] Ma, H.; Weiss, M.; Malik, D.; Berthelot, B.; Yebra, M.; Nolan, R.H.; Mialon, A.; Zeng, J.; Quan, X.; Tagesson, H.T.; et al. Satellite Canopy Water Content from Sentinel-2, Landsat-8 and MODIS: Principle, Algorithm and Assessment. Remote Sens. Environ. 2025, 326, 114801, doi:10.1016/j.rse.2025.114801.

[30] Tsele, P.; Ramoelo, A.; Moleleki, L.; Laurie, S.; Mphela, W.; Tshuma, N. Leaf Area Index-Based Phenotypic Assessment of Sweet Potato Varieties Using UAV Multispectral Imagery and a Hybrid Retrieval Approach. Smart Agric. Technol. 2025, 11, 100960, doi:10.1016/j.atech.2025.100960.

[31] Yao, Y.; Wang, H.; Yang, X.; Gao, X.; Yang, S.; Zhao, Y.; Li, S.; Zhang, X.; Liu, Z. Interpretable LAI Fine Inversion of Maize by Fusing Satellite, UAV Multispectral, and Thermal Infrared Images. Agriculture 2025, 15, 243, doi:10.3390/agriculture15030243.

[32] Fan, W.; Wu, J.; Zheng, G.; Zhang, Q.; Xu, X.; Du, H.; Zheng, M.; Zhang, K.; Zhang, F. Retrieving the Leaf Area Index of Dense and Highly Clumped Moso Bamboo Canopies from Sentinel-2 MSI Data. Remote Sens. 2025, 17, 1891, doi:10.3390/rs17111891.

[33] Miranda, R.D.Q.; Nóbrega, R.L.B.; Moura, M.S.B.D.; Raghavan, S.; Galvíncio, J.D. Realistic and Simplified Models of Plant and Leaf Area Indices for a Seasonally Dry Tropical Forest. Int. J. Appl. Earth Obs. Geoinformation 2020, 85, 101992, doi:10.1016/j.jag.2019.101992.

[34] Ma, B.; Xu, M. Identifying Outliers of the MODIS Leaf Area Index Data by Including Temporal Patterns in Post-Processing. Remote Sens. 2023, 15, 5042, doi:10.3390/rs15205042.

[35] Ji, J.; Li, X.; Du, H.; Mao, F.; Fan, W.; Xu, Y.; Huang, Z.; Wang, J.; Kang, F. Multiscale Leaf Area Index Assimilation for Moso Bamboo Forest Based on Sentinel-2 and MODIS Data. Int. J. Appl. Earth Obs. Geoinformation 2021, 104, 102519, doi:10.1016/j.jag.2021.102519.

[36] Alexandridis, T.K.; Ovakoglou, G.; Clevers, J.G.P.W. Relationship between MODIS EVI and LAI across Time and Space. Geocarto Int. 2020, 35, 1385–1399, doi:10.1080/10106049.2019.1573928.

[37] Ganguly, S.; Samanta, A.; Schull, M.; Shabanov, N.; Milesi, C.; Nemani, R.; Knyazikhin, Y.; Myneni, R. Generating Vegetation Leaf Area Index Earth System Data Record from Multiple Sensors. Part 2: Implementation, Analysis and Validation. Remote Sens. Environ. 2008, 112, 4318–4332, doi:10.1016/j.rse.2008.07.013.

[38] Yuan, W.; Liu, S.; Yu, G.; Bonnefond, J.-M.; Chen, J.; Davis, K.; Desai, A.R.; Goldstein, A.H.; Gianelle, D.; Rossi, F.; et al. Global Estimates of Evapotranspiration and Gross Primary Production Based on MODIS and Global Meteorology Data. Remote Sens. Environ. 2010, 114, 1416–1431, doi:10.1016/j.rse.2010.01.022.